Control of coexisting magnetic phases by electric fields in NdFe₃(BO₃)₄

S. Partzsch,[1,*] J.-E. Hamann-Borrero,[1,†] C. Mazzoli,[2,3] J. Herrero-Martin,[2,4] S. Valencia,[5] R. Feyerherm,[5] E. Dudzik,[5]
A. Vasiliev,[6,7,8] L. Bezmaternykh,[9] B. Büchner,[1,10] and J. Geck[11]

[1]*Leibniz Institute for Solid State and Materials Research IFW Dresden, Helmholtzstrasse 20, D-01069 Dresden, Germany*
[2]*European Synchrotron Radiation Facility (ESRF), BP 220, 38043 Grenoble, France*
[3]*Dipartimento di Fisica e Unità CNISM, Politecnico di Milano, Piazza Leonardo Da Vinci 32,I-20133 Milano, Italy*
[4]*ALBA Synchrotron Light Source, E-08290 Cerdanyola del Vallès, Barcelona, Spain*
[5]*Helmholtz Zentrum Berlin. Albert Einstein Str.15 12489 Berlin, Germany*
[6]*Low Temperature Physics Department, Faculty of Physics, Moscow State University, Moscow 119992, Russia*
[7]*Theoretical Physics and Applied Mathematics Department, Ural Federal University, 620002 Ekaterinburg, Russia*
[8]*National University of Science and Technology "MISiS", Moscow 119049, Russia*
[9]*L. V. Kirensky Institute of Physics, Siberian Branch of RAS, Krosnayarsk 660036, Russia*
[10]*Institute for Solid State Physics, Dresden Technical University, TU-Dresden, D-01062 Dresden, Germany*
[11]*Paris Lodron University Salzburg, Chemistry and Physics of Materials, Hellbrunner Str. 34, 5020 Salzburg, Austria*

We present a resonant x-ray diffraction study of the magnetic order in NdFe₃(BO₃)₄ and its coupling to applied electric fields. Our high-resolution measurements reveal two different coexisting magnetic phases, which can directly be controlled and manipulated by external electric fields. More specifically, the volume fraction of the collinear magnetic phase is found to strongly increase at the expense of helically ordered regions when an electric field is applied. These results confirm that the collinear magnetic phase is responsible for the ferroelectric polarization of NdFe₃(BO₃)₄ and, more importantly, demonstrate that coexisting magnetic phases provide a route towards materials with a strong but yet hysteresis-free magnetoelectric response.

I. INTRODUCTION

Frustrated magnetic materials exhibit a large variety of intriguing physical phenomena, including the concomitant appearance of coupled ferroelectric and magnetic orders [1,2]. In fact, interlinked magnetic and ferroelectric orders are very rare in nature. Their discovery in various frustrated magnets was therefore a surprise and generated a lot of excitement [3,4], not only because these phenomena are very interesting from the viewpoint of basic research. There is also a significant technological potential [5,6], especially since a strong magnetoelectric coupling enables us to store information in an energy-efficient way [7,8] or to design novel magnetoelectric sensors and oscillators [9]. Although microscopic information of how electric fields modify magnetic orders still remains rare, earlier experiments could demonstrate the manipulation of magnetic order using electric fields [10–13]. These studies, however, focused on electric field induced changes within a single magnetic phase.

In the present work we consider a different situation, where magnetic frustration results in two distinct but metastable coexisting magnetic phases. In this case, the effect of the electric field on the magnetism is not due to the ME coupling within one of those phases but due to their field-controlled volume fractions.

As a case in point, we study the electric field dependence of the magnetic order in NdFe₃(BO₃)₄, which is a frustrated magnetic material with a large magnetoelectric (ME)

response [14]. We find that an applied electric field has a dramatic effect on the microscopic magnetic state of the material. More specifically, we show that the ME effect of NdFe₃(BO₃)₄ is due to manipulating the volume fractions of two coexisting phases with distinct magnetic orderings. We further demonstrate that the ME response does not exhibit any significant field hysteresis. While this is unfavorable for nonvolatile memory applications, the absence of a hysteresis is essential for ME sensors and oscillators [9].

The rhombohedral lattice structure of this material is illustrated in Fig. 1, where, for the sake of simplicity, only the two magnetic sublattices of Fe and Nd are shown. These two sublattices are magnetically coupled and undergo two magnetic phase transitions as a function of temperature [16–18]: Upon cooling, commensurate magnetic (CM) order sets in first at $T_N \approx 30$ K. In this phase the spins are ordered in a collinear fashion, forming ferromagnetic (FM) ab planes, which are coupled antiferromagnetically (AFM) along the c direction. The magnetic modulation vector is commensurate, causing magnetic superlattice peaks at $\mathbf{q}_{CM} = (0,0,3n + 3/2)$ with integer n. Below $T_{IC} \approx 15$ K, a continuous transition into an incommensurate magnetic (ICM) phase occurs, where the FM moments of the ab planes form helices propagating along the c direction. The helical order is signaled by magnetic superlattice peaks at $\mathbf{q}_{ICM} = (0,0,3n + 3/2 \pm \delta)$, where δ increases continuously with further cooling due to a dramatically decreasing period of the spin helix ranging from $523 \times c$ at 14 K down to $146 \times c$ at 1.6 K.

Interestingly, applying an external magnetic field $B_a \approx 1.3$ T at 4.8 K along the a direction induces an electric polarization $\mathcal{P}_a$ of up to 400 μC/m² along the same axis [14]. This strong magnetoelectric coupling sparked significant interest in NdFe₃(BO₃)₄ and immediately raised the question about

---

*Present address: Optotransmitter und Umweltschutz-technologie OUT e.V., Köpenicker Str. 325, Haus 201, D-12555 Berlin, Germany.
†j.e.hamann.borrero@ifw-dresden.de
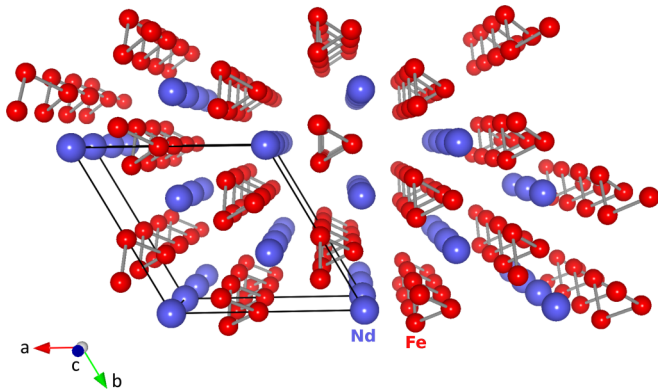
FIG. 1. Crystal structure of $NdFe_3(BO_3)_4$. The material can be described using the rhombohedral space group $R32$ with hexagonal unit cell parameters $a = 9.578$ Å and $c = 7.605$ Å at room temperature [15]. Only the magnetic sublattices of Fe (red) and Nd (purple) are shown. Fe is coordinated by oxygen octahedra, which form edge sharing helical chains along the c-direction. These chains and NdO_6 triangular prisms are connected in the ab-plane by BO_3 triangles (not shown).

its microscopic origin. Recent x-ray diffraction experiments already provided microscopic insight and implied that the finite $\mathcal{P}_a$ is related to the magnetic field-induced CM order [18,19]. In principle, the strong magnetoelectric coupling discovered in previous studies should also enable us to alter the magnetic order of $NdFe_3(BO_3)_4$ by applying external electric fields. Yet no experimental studies of this effect have been available up to now. We therefore performed high-resolution magnetic resonant x-ray diffraction (RXD) in applied electric fields in order to close this gap.

II. EXPERIMENT

The magnetic RXD in applied electric fields has been performed at the resonant scattering beamline of the

European Synchrotron Radiation Facility (ESRF) in Grenoble, France [20]. A liquid helium orange cryostat equipped with an E-field stick—in-house built by one of us (C.M.)—was mounted on a six circle diffractometer as described in Refs. [11] and [21], using a horizontal scattering geometry. The sample with a thickness of 1.3 mm along the a direction was mounted between two vertical electrodes, leaving an additional gap of 0.5 mm between the top electrode and the $NdFe_3(BO_3)_4$ crystal. By applying a voltage across the two electrodes, electric fields up to $E = 88$ kV/m parallel to the crystallographic a axis were generated. We set the photon energy to the Nd L_2 edge at 6.726 keV in order to probe the magnetic order of the Nd sublattice, which, in turn, also reflects the magnetic order of the Fe sublattice [18]. For the L scans shown in the following, the incoming light was horizontally (π) polarized and no polarization analyzer was used. Additional RXD measurements as a function of magnetic field have been performed employing the MagS beamline at the BESSY synchrotron of the Helmholtz-Zentrum Berlin using its six plus three circle Eulerian cradle equipped with a superconducting magnet. The magnetic field was applied parallel to the crystallographic a direction and the RXD was again done at the Nd L_2, this time employing a vertical scattering geometry and horizontally (σ) polarized light.

III. RESULTS

In Fig. 2, L scans through the magnetic superlattice reflections measured at 5.8 K are presented. These data sets have been analyzed by fitting three Lorentzian squared functions plus a linear background to the measured intensity profiles, yielding the full width at half maximum (FWHM) as well as the integrated intensities (area under the different Lorentzian squared functions) for the three observed peaks. The values reported in the following refer to these fitted quantities and their confidence intervals.

Prior to these measurements the state of the sample was prepared by cooling down to 5.8 K without electric field. The
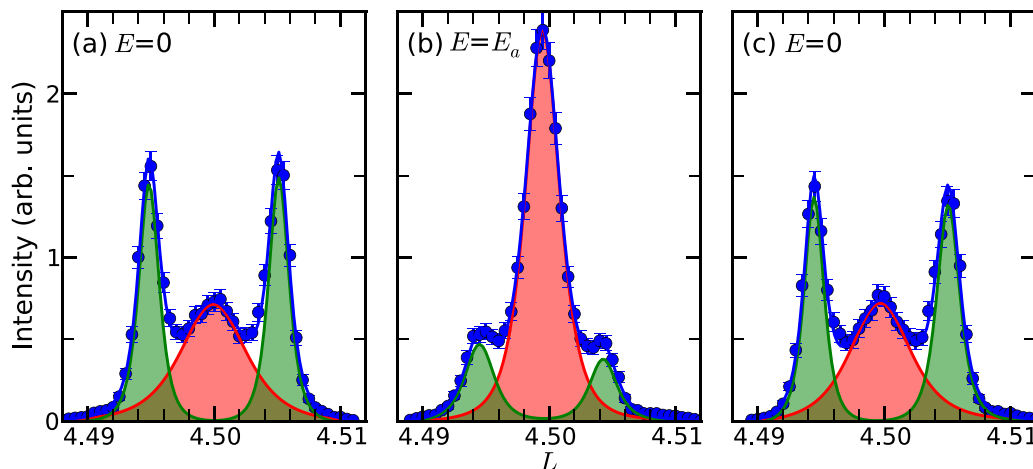
FIG. 2. E-field dependence of the L scans around the (0 0 4.5) position at 5.8 K, fitted by three Lorentzian squared functions plus a linear background. The separate peaks of the fit are shown as green and red lines, representing the ICM (green) and CM satellites (red). The sum of the fitted peaks and the linear background (blue line) agrees well with the experimental data (blue dots). (b) Upon applying a moderate electric field of $E_a = 88$ kV/m, a dramatic change in the magnetic scattering is observed. (c) After removing E, the initial intensity profile is recovered, i.e., the process is reversible.
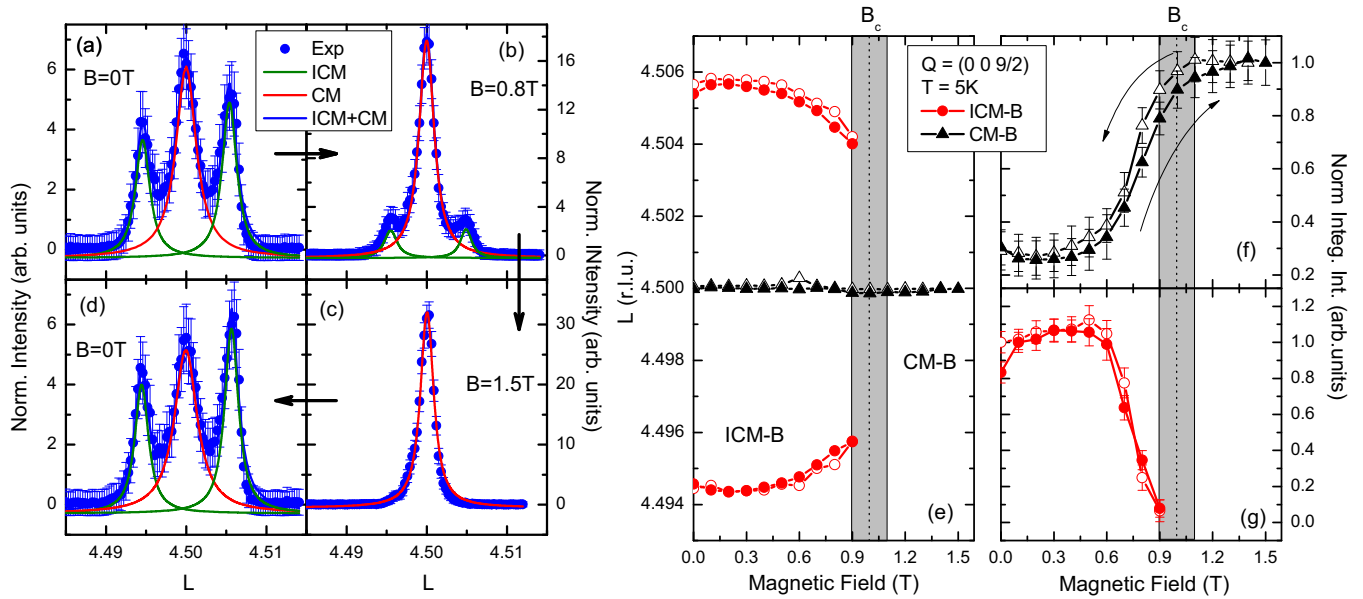
FIG. 3. Magnetic field dependence of magnetic satellite reflections around (0,0,4.5) at 5 K. (a)–(d): L scans through the (0,0,4.5) peak at various magnetic fields. The magnetic field induced changes closely correspond to the ones induced by electric fields (cf. Fig. 2). The solid lines represent again fits to the data. Extracted fit parameters as a function of applied magnetic field are presented in (e)–(g). Field loops up to 1.5 T and back to 0 T are shown. (e) Position of the CM and ICM peaks, (f) integrated intensity of the CM peak, and (g) total integrated intensity of the ICM satellites at $\pm\delta$. In none of the measurements a clear hysteresis appears. The critical field B_c is defined by the disappearance of the ICM satellites, where the shaded region indicates the uncertainty of our experiment.

L scan obtained for this zero field cooled state is shown in Fig. 2(a). In agreement with previous results both the (0, 0, 4.5) of the CM phase as well as the ICM satellites at $(0,0,4.5 \pm \delta)$ are observed, revealing the coexistence of the CM minority and the ICM majority phase under the present conditions. The effect of an electric field on this phase coexistence can clearly be observed in Fig. 2(b). Applying $E_a = 88$ kV/m results in a transfer of intensity from the ICM satellites to the central CM reflection, during which the sum of the integrated intensities from the IC and the CM domains stays constant within 5%. The E field also has a corresponding effect on the FWHM of the superlattice reflections, which measures the average correlation length of the CM and ICM ordered regions. The E-field dependence of the FWHM has been extracted from the fitted curves in Fig. 2. At 5.8 K and $E_a = 0$ V/m the width of the ICM satellites is found to be resolution limited (FWHM = $0.001 \times 2\pi/c$), as determined by comparison to the FWHM of the neighboring (006) Bragg reflection. This implies a correlation length $\xi_{ICM} > 760$ nm. Increasing the electric field to $E_a = 88$ kV/m causes a clear reduction of ξ_{ICM} to (480 ± 30) nm (FWHM increases from $0.001 \times 2\pi/c$ to $0.0016 \times 2\pi/c$). Conversely, the correlation length of the CM-ordered regions increases with E_a from $\xi_{CM} = (200 \pm 20)$ nm at $E_a = 0$ V/m to $\xi_{CM} = (450 \pm 25)$ nm at $E_a = 88$ kV/m (FWHM decreases from $0.0037 \times 2\pi/c$ to $0.0017 \times 2\pi/c$). The concomitant changes of the integrated intensities and the correlation lengths immediately imply that the electric field stabilizes the CM phase and increases its volume fraction at the expense of the ICM phase. The stabilization of the CM phase by an applied electric field further reveals that the electric moment of this phase must be larger than that of the ICM phase. In fact, the comparison to macroscopic measurements

indicates that only the CM phase is ferroelectric while the ICM phase does not possess a significant $\mathcal{P}$ [22]. It is important to realize that a manipulation of phase fractions has so far only been achieved very close to a phase transition. For instance between T_C and $0.95 \times T_C$ in Ref. [13], whereas here we observe much larger effects even at $0.3 \times T_{IC}$.

However, the transformation from the ICM to the CM phase is not complete within the studied E field range, as incommensurate reflections always retain a significant intensity. After the E field is switched off, the zero field state is recovered, as demonstrated in Fig. 2(c). Hence the effect of the applied E field is reversible, and our results do not show any significant hysteresis.

A complete transformation into the CM phase can be much more easily achieved by applying magnetic fields up to 1.5 T, as shown in Fig. 3. Similar to the measurements as a function of E, for all B fields we observe the central CM peak, implying the coexistence of the ICM and CM phase below B_c. In addition, the magnetic field dependencies also show no hysteresis within the experimental errors, i.e., the field-driven ICM-CM transitions are largely reversible and continuous, as are the temperature-driven transitions [17,18]. In the absence of a discontinuous transition, the observed phase coexistence down to 5 K corresponding to $0.3 \times T_{IC}$ or $0.2 \times T_N$ is very surprising. These observations can, however, be interpreted consistently in terms of pinned CM domains that survive deep inside the ICM phase. Such CM domains will act as seeds for the CM phase, which effectively flatten nucleation barriers and thereby reduce hysteretic behavior [23].

Note also that the ICM-CM transition as a function of field and as a function of temperature proceeds very differently: While δ as a function of field at constant temperature always
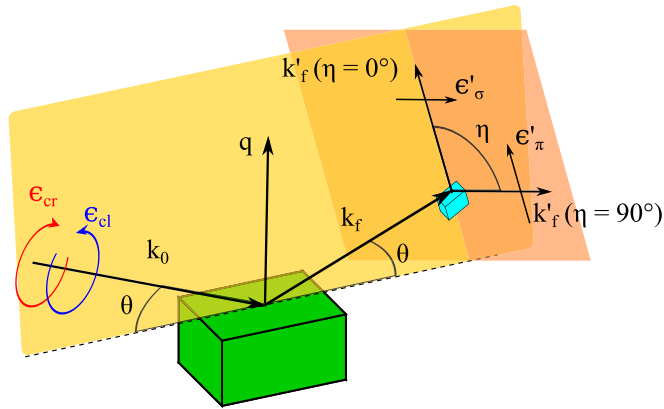
FIG. 4. Scattering geometry used during the Stokes analysis. The incoming photon with wave vector k_0 is circularly right (ϵ_{cr}) or left (ϵ_{cl}) polarized. The scattered beam with wave vector k_f is again diffracted by the analyzer crystal, shown in blue. The scattered x ray is linearly polarized ϵ'. By rotating the analyzer crystal an angle η about the direction given by k_f, different components of the scattered beam polarization are selected, e.g., ϵ'_π for $\eta = 90°$ and ϵ'_σ for $\eta = 0°$. **q** is the scattering vector and θ the Bragg angle.

remains finite (cf. Figs. 2 and 3), it rapidly approaches zero upon warming [17,18]. In other words, while the ICM modulation at a fixed temperature only weakly couples to external fields, it transforms smoothly into the CM modulation upon warming in zero field. Thus, at a fixed temperature, the system can only change between ICM ($\delta \neq 0$) and CM ($\delta = 0$) by adjusting the respective volume fractions, fully consistent with the conclusions presented above. Our results therefore in particular show that the magnetic response to an electric field is based on two distinct but coexisting magnetic phases, whose volume fractions are controlled by E. This is distinctly different from effects reported earlier, where the magnetoelectric effect was dominated by the intrinsic response of a single magnetic phase [10–13].

In order to get further microscopic information about the magnetic state under the various studied conditions, we performed a polarization analysis of the magnetic RXD by means of so-called Stokes scans, which are described in more detail in the appendix and which are illustrated in Fig. 4. During these scans, both the polarization of the incoming and the detected photons are controlled. The incoming beam polarization was set to circular right (c_r) or circular left (c_l), using a diamond phase plate, whereas the polarization of the scattered beam was characterized using a Cu220 analyzer. More specifically, the polarization of the scattered beam was characterized by rotating the polarization analyzer about the scattered beam direction by an angle η, where $\eta = 0°$ and $\eta = 90°$ correspond to a final polarization perpendicular and parallel to the scattering plane, respectively (see Fig. 4). These measurements yield the integrated intensity of the magnetic RXD as a function of η and the incoming beam polarization, which provides detailed information about the symmetry of the probed magnetic order [24–26].

In this way, we investigated four different states: (i) the CM phase in zero fields at 20 K (CM-T), (ii) zero field ICM at 5.8 K (ICM), (iii) the CM phase induced by applied magnetic field at 2 K and $B_a = 2$ T (CM-B, cf. Fig. 3), as well as (iv) the
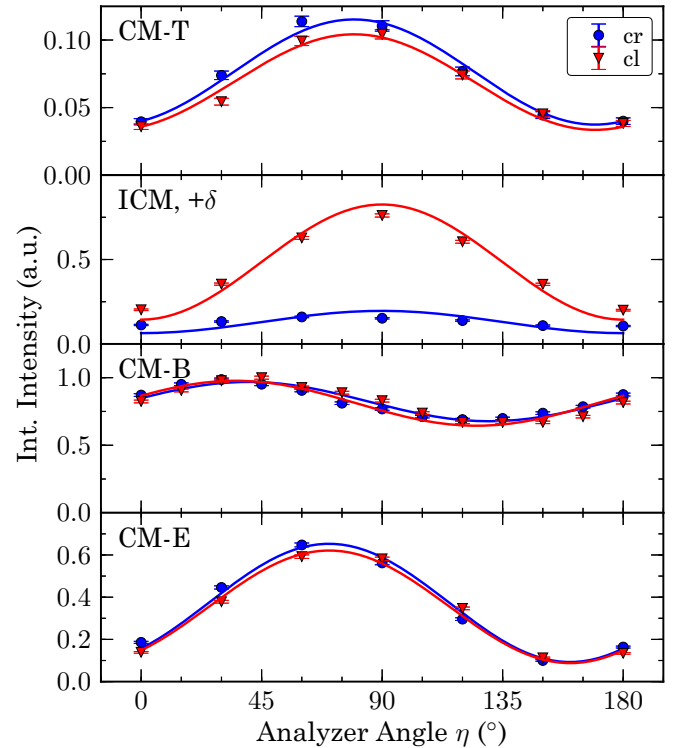
FIG. 5. Comparison of experimental (symbols) and simulated (lines) Stokes scans for circular right (c_r) and circular left (c_l) polarized incoming photons. The measured superlattice peaks are (0 0 7.5) and (0 0 7.5 + δ) for CM and ICM, respectively. Temperature and fields for the shown measurements are: CM-T: 20 K, no field. ICM: 5.8 K, no field. CM-B: 2 K, 2 T. CM-E: 5.8 K, 88 kV/m.

CM phase induced by applied electric field $E_a = 88$ kV/m at 5.8 K (CM-E, cf. Fig. 2).

In order to extract information about the microscopic magnetic configuration of the sample, the experimental data shown in Fig. 5 were compared to model calculations. For the models we used the leading first order term of the scattering tensor, $\hat{f}^{(1)}$ [27,28], which, in the present symmetry, has the standard from $\hat{f}_{ij}^{(1)} \propto \epsilon_{ijk}m_k$, where ϵ_{ijk} and m_k are the totally antisymmetric third rank tensor and the magnetic moment direction, respectively [29]. Further details regarding the model calculations can be found in the appendix. For the CM-T phase we find that the polarization dependent magnetic RXD cannot be described by a monodomain state. Instead, three domains are necessary to reproduce the experimental data (top row in Fig. 5). While these measurements do not allow us to determine the absolute spin directions of the different magnetic domains, we find that they must be rotated by 120° with respect to one another in the ab plane. This is expected because of the threefold axis of the unperturbed lattice structure (neglecting the small ferroelectric distortion).

The onset of the ICM order is signaled by the appearance of the IC satellites, which exhibit different resonant intensities for c_r and c_l (second panel from top in Fig. 5). This difference is due to the chirality of the magnetic helix. Specifically, our analysis yields the expected presence of left- and right-handed domains with volume fractions of (0.74 ± 0.02) and (0.26 ± 0.02), respectively.

The above findings for the CM-T and ICM phase are in good agreement with neutron scattering results [16,17]. It was also shown earlier that a magnetic field of 2 T applied to the CM phase suffices to create a monodomain CM-B state [18,19]. Our analysis of the Stokes scans yields the same result, using a different and independent method. The above comparison to previous studies hence verifies our approach and shows that the full polarization control in magnetic RXD provides a powerful means to identify and characterize magnetic multidomain states.

Turning to the CM-E, we again find that three magnetic domains with a relative angle of 120° are necessary to model the experimental data, very similar to the case of the CM-T state described above. Our maximum electric field of 88 kV/m therefore does not create a monodomain state with collinear magnetic order along one single direction. Instead still different types of domains are found to exist. This is in contrast to the monodomain CM-B state described above.

IV. SUMMARY

In summary, the key result of the present work is the observation of a delicate balance between two distinct magnetic phases, which reacts very sensitively to an applied electric field. More specifically, the present magnetic RXD experiments reveal a complex microscopic state, where the coexisting CM and ICM regions also realize different domain types, namely three 120° CM and two left/right-handed ICM domains. Within the errors of the present experiment, the field-controlled ICM-CM transition is reversible. This can be explained by the observed presence of pinned CM domains, which act as nucleation seeds for the phase transformation. It is important to point out that frustrated magnetic couplings result in the competition of the CM and ICM order [18]. Hence, this frustration also underlies the coexisting magnetic phases reported here, which occur deep inside the ICM phase even in the absence of a strong first order transition. Controlling magnetic phase separation in frustrated materials by electric fields and pinning centers therefore provides an alternative route towards new materials with a large and hysteresis-free ME response.

APPENDIX

1. Stokes scans analysis

In order to determine the various magnetic structures of NdFe$_3$(BO$_3$)$_4$ under the different experimental conditions,

we have performed a polarization analysis of the scattered beam by means of so-called Stokes scans [11,21]. The scattering geometry used during this analysis is shown in Fig. 4. The incoming beam polarization was set to circularly right (c_r) or left (c_l) using a diamond phase plate. The polarization state of the incoming radiation, as characterized by the measured polarization parameters ($P_1, P_2, |P_3|$) [24], was (0.030, −0.006, 1.000) and (0.042, −0.008, 0.999) for circular left and circular right, respectively, showing the high degree of circular polarization. The polarization of the scattered beam k_f was then monitored using a Cu220 analyzer, which can be rotated about the direction of the scattered beam by an angle η. This η defines the linear polarization direction of the photons that finally reach the detector behind the analyzer (cf. Fig. 4). For $\eta = 0°$ the polarization corresponds to σ' and $\eta = 90°$ to π' (cf. Fig. 4).

For different **q** vectors corresponding to the different magnetic modulations we have integrated rocking scans of the analyzer crystal at each η to obtain the integrated intensity $I_\mathbf{q}(\eta)$. The measured intensity $I_\mathbf{q}(\eta)$ at the wave vector **q** is given by

$$I_\mathbf{q}(\eta) \propto \left| \sum_{j=1}^{M} \hat{f}_j(\mathbf{q},\eta) e^{i\mathbf{q}\cdot\mathbf{r}_j} \right|^2, \tag{A1}$$

$\hat{f}_j(\mathbf{q},\eta)$ being the atomic scattering tensor and $\mathbf{r}_j$ the position coordinate of site j.

Since in NdFe$_3$(BO$_3$)$_4$ the magnetic moments are parallel to the ab plane [16–18] and there is a threefold axis along c, only the leading first order term of the spherical harmonic expansion of the scattering tensor $F^{(1)}$ enters at the AFM superlattice positions [27,28], allowing us to apply the usual formalism given in Ref. [29].

$$\hat{f}_j^{(1)}(\mathbf{q},\eta) \propto (\epsilon'^*(\eta) \times \epsilon) \cdot \hat{\mathbf{m}}_j, \tag{A2}$$

where $\hat{\mathbf{m}}_j$ is the magnetic moment direction at site j, and $\epsilon = c_r, c_l$ is the incoming and $\epsilon'(\eta)$ is the outgoing polarization vector.

2. Commensurate magnetic structures

a. Analysis of the CM-T state

The magnetic structure of the Nd sublattice in the CM-T state can be described as

$$\hat{\mathbf{m}}_j = (-1)^j (\hat{\mathbf{a}} \cos\phi_0 + \hat{\mathbf{b}} \sin\phi_0), \tag{A3}$$

where $\hat{\mathbf{a}}$ is the unit vector along the a direction and $\hat{\mathbf{b}}$ is the unit vector along $\mathbf{a} \times \mathbf{c}$. Note that $\hat{\mathbf{b}}$ is not a lattice vector. The angle ϕ_0 is a degree of freedom used during the fitting procedure and allows us to check for possible tilting angles of the magnetic moment away from the ideal crystallographic direction a.

Due to the threefold axis of the space group $R32$, the a axis can have three equivalent directions in the hexagonal basal plane separated by an angle of 120° from each other. This yields three possible magnetic domains. The presence of different domains is already revealed by comparing the experimentally determined polarization parameters of the scattered beam to single magnetic domain models via Eqs. (A1) and (A2). Such a comparison for the CM-T state is shown
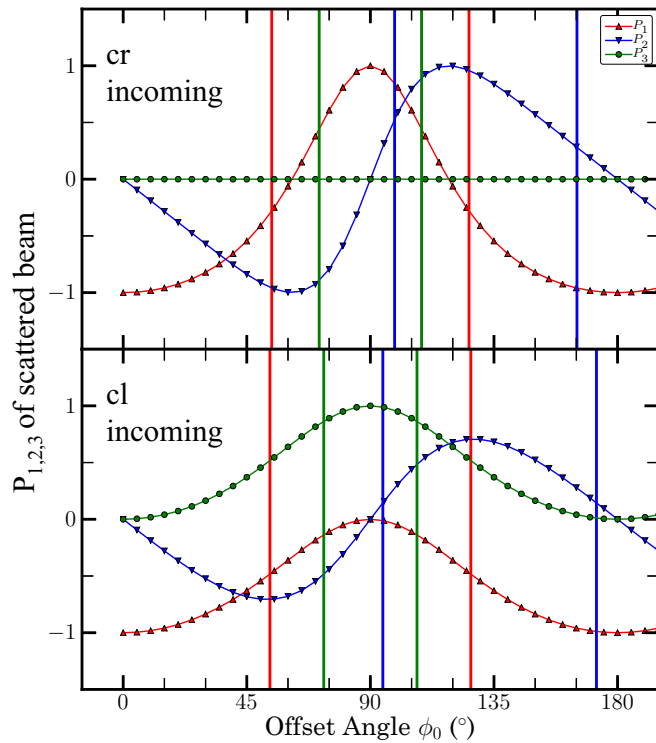
FIG. 6. Comparison of the calculated and observed $P_{1,2,3}$ of the scattered beam for the (0,0,7.5) reflection at the Nd L_2 edge, measured with circular right (cr) and circular left (cl) polarized incoming light. The curves were calculated using a monodomain model by varying the value of ϕ_0. The vertical lines indicate the ϕ_0 values at which the calculated $P_{1,2,3}$ matches the corresponding experimental value.

in Fig. 6, where the polarization parameters for the scattered beam are shown as a function of ϕ_0 for a monodomain model. The vertical lines in the figure represent the ϕ_0 value at which the calculated $P_{1,2,3}$ curve coincides with the experimental $P_{1,2,3}$ value. As can be seen in the figure, there is no single ϕ_0, which enables us to reproduce all three polarization parameters at the same time. This shows that a monodomain model is not able to reproduce the experimental data and verifies the presence of several domains.

If the x-ray beam coherence or experimental resolution is smaller than the domain size the phase relation between the domains has not to be considered and their diffracted intensities $I_{\mathbf{q}}^d(\eta)$ add up incoherently, i.e., without interferences. In this case, the total magnetic scattering intensity is:

$$I_{\mathbf{q}}^T(\eta) = \sum_{n=1}^{3} d_n \, I_{\mathbf{q}}^{d_n}(\eta), \tag{A4}$$

where d_n is the domain fractional occupation with respect to the volume probed by the x-ray beam.

During the calculation of the scattered intensities using Eq. (A1), three domains with occupations d_1, d_2, and d_3

were considered with angles of ϕ_0, $\phi_0 + 120°$, and $\phi_0 + 240°$, respectively. In full agreement with neutron [16] and x-ray diffraction [19] reports, the best fit result was obtained with a multidomain structure with occupation $d_1 = (0.27 \pm 0.02)$, $d_2 = (0.50 \pm 0.02)$, and $d_3 = (0.23 \pm 0.02)$ and $\phi_0 = 0$ deg. We note that the present analysis in principle allows for monodomain solutions (cf. analysis of the CM-B state). However, in accordance with the analysis of the polarization parameters described above, monodomain models cannot reproduce the Stokes scans. This was verified by enforcing $d_1 = 1$ and $d_2 = d_3 = 0$.

b. Analysis of the CM-B state

The CM-B state was analyzed analogous to the CM-T state, using the magnetic structure as defined by Eq. (A3). The best fit to the experimental data yielded a single domain structure, where the Nd moments are tilted an angle $\phi_0 = 95°$ away from the a direction. The obtained ϕ_0 enables us to reproduce all the experimental polarization parameters.

The moments therefore align perpendicular to the applied magnetic field $\mathbf{B}_a$, i.e., perpendicular to a. Again, this result is in agreement with previous observations [19]. The discrepancy with the expected 90° angle can be explained by the experimental misalignment by 5° of the applied magnetic field with respect to the crystallographic a direction.

c. Analysis of the CM-E state

Also the CM-E state was analyzed employing the magnetic structure defined by Eq. (A3). The same analysis already applied to the CM-T state shows that monodomain models are unable to capture the experimental results. The best description of the experiment is given by a multidomain structure similar to that observed in the CM-T state but with a domain occupation of $d_1 = (0.31 \pm 0.02)$, $d_2 = (0.61 \pm 0.02)$, and $d_3 = (0.08 \pm 0.02)$. Here, the domain with the highest occupation is that with its moments' directions closest to the direction perpendicular to the electric field $\mathbf{E}_a$.

3. Incommensurate magnetic structure

For the analysis of the magnetic intensities of the incommensurate magnetic structure, we have used the magnetic structure determined from neutron diffraction [17], which can be described as

$$\hat{\mathbf{m}}_j = \hat{\mathbf{a}} \cos(2\pi \mathbf{q} \cdot \mathbf{r}_j) + \hat{\mathbf{b}} \sin(2\pi \mathbf{q} \cdot \mathbf{r}_j). \tag{A5}$$

Note that two possible magnetic helical structures can emerge depending on the handedness of the pitch rotation of the helix. The fitting of the satellites around **q** vectors (0 0 4.5) and (0 0 7.5) leads finally to a multidomain helical structure with $d_1 = (0.74 \pm 0.02)$ for right-handed and $d_2 = (0.26 \pm 0.02)$ for left-handed helices.

---

[1] S.-W. Cheong and M. Mostovoy, Nat. Mater. **6**, 13 (2007).

[2] D. Khomskii, Physics **2**, 20 (2009).

[3] T. Kimura, T. Goto, H. Shintani, K. Ishizaka, T. Arima, and Y. Tokura, Nature (London) **426**, 55 (2003).

[4] N. Hur, S. Park, P. A. Sharma, J. S. Ahn, S. Guha, and S.-W. Cheong, Nature (London) **429**, 392 (2004).

[5] R. Ramesh and N. A. Spaldin, Nat. Mater. **6**, 21 (2007).

[6] J. Ma, J. Hu, Z. Li, and C.-W. Nan, Adv. Mater. **23**, 1062 (2011).

[7] C. A. F. Vaz, J. Phys.: Condens. Matter **24**, 333201 (2012).

[8] J. T. Heron, D. G. Schlom, and R. Ramesh, Appl. Phys. Rev. **1**, 021303 (2014).

[9] Y. S. Oh, S. Artyukhin, J. J. Yang, V. Zapf, J. W. Kim, D. Vanderbilt, and S.-W. Cheong, Nat. Commun. **5**, 3201 (2014).

[10] P. G. Radaelli, L. C. Chapon, A. Daoud-Aladine, C. Vecchini, P. J. Brown, T. Chatterji, S. Park, and S.-W. Cheong, Phys. Rev. Lett. **101**, 067205 (2008).

[11] F. Fabrizi, H. C. Walker, L. Paolasini, F. de Bergevin, A. T. Boothroyd, D. Prabhakaran, and D. F. McMorrow, Phys. Rev. Lett. **102**, 237205 (2009).

[12] Y. Tokunaga, Y. Taguchi, T.-h. Arima, and Y. Tokura, Nat. Phys. **8**, 838 (2012).

[13] Y. Bodenthin, U. Staub, M. García-Fernández, M. Janoschek, J. Schlappa, E. I. Golovenchits, V. A. Sanina, and S. G. Lushnikov, Phys. Rev. Lett. **100**, 027201 (2008).

[14] A. Zvezdin, A. Kadomtseva, S. Krotov, A. Pyatakov, Y. Popov, and G. Vorob'ev, J. Magn. Magn. Mater. **300**, 224 (2006), the third Moscow International Symposium on Magnetism 2005.

[15] J. A. Campá, C. Cascales, E. Gutiérrez-Puebla, M. A. Monge, I. Rasines, and C. Ruíz-Valero, Chem. Mater. **9**, 237 (1997).

[16] P. Fischer, V. Pomjakushin, D. Sheptyakov, L. Keller, M. Janoschek, B. Roessli, J. Schefer, G. Petrakovskii, L. Bezmaternikh, V. Temerov, and D. Velikanov, J. Phys.: Condens. Matter **18**, 7975 (2006).

[17] M. Janoschek, P. Fischer, J. Schefer, B. Roessli, V. Pomjakushin, M. Meven, V. Petricek, G. Petrakovskii, and L. Bezmaternikh, Phys. Rev. B **81**, 094429 (2010).

[18] J. E. Hamann-Borrero, S. Partzsch, S. Valencia, C. Mazzoli, J. Herrero-Martin, R. Feyerherm, E. Dudzik, C. Hess, A. Vasiliev, L. Bezmaternykh, B. Büchner, and J. Geck, Phys. Rev. Lett. **109**, 267202 (2012).

[19] J. E. Hamann-Borrero, M. Philipp, O. Kataeva, M. v. Zimmermann, J. Geck, R. Klingeler, A. Vasiliev, L. Bezmaternykh, B. Büchner, and C. Hess, Phys. Rev. B **82**, 094411 (2010).

[20] L. Paolasini, C. Detlefs, C. Mazzoli, S. Wilkins, P. P. Deen, A. Bombardi, N. Kernavanois, F. de Bergevin, F. Yakhou, J. P. Valade, I. Breslavetz, A. Fondacaro, G. Pepellin, and P. Bernard, J. Synchrotron Radiat. **14**, 301 (2007).

[21] H. C. Walker, F. Fabrizi, L. Paolasini, F. de Bergevin, J. Herrero-Martin, A. T. Boothroyd, D. Prabhakaran, and D. F. McMorrow, Science **333**, 1273 (2011).

[22] A. Zvezdin, G. Vorob'ev, A. Kadomtseva, Y. Popov, A. Pyatakov, L. Bezmaternykh, A. Kuvardin, and E. Popova, JETP Lett. **83**, 509 (2006).

[23] H. Vehkamaeki, *Classical Nucleation Theory in Multicomponent Systems* (Springer-Verlag, Berlin, Heidelberg, 2006).

[24] C. Detlefs, M. S. d. Rio, and C. Mazzoli, Eur. Phys. J. Special Topics **208**, 359 (2012).

[25] C. Mazzoli, S. B. Wilkins, S. Di Matteo, B. Detlefs, C. Detlefs, V. Scagnoli, L. Paolasini, and P. Ghigna, Phys. Rev. B **76**, 195118 (2007).

[26] R. D. Johnson, S. R. Bland, C. Mazzoli, T. A. W. Beale, C.-H. Du, C. Detlefs, S. B. Wilkins, and P. D. Hatton, Phys. Rev. B **78**, 104407 (2008).

[27] J. P. Hannon, G. T. Trammell, M. Blume, and D. Gibbs, Phys. Rev. Lett. **61**, 1245 (1988).

[28] M. W. Haverkort, N. Hollmann, I. P. Krug, and A. Tanaka, Phys. Rev. B **82**, 094403 (2010).

[29] J. P. Hill and D. F. McMorrow, Acta Crystallogr. Sect. A **52**, 236 (1996).